LA-UR-15-25960
Approved for public release; distribution is unlimited.

Title: Azimuthal Sampling of Tectonic Release from Rayleigh Waves, Triggered by Shallow Explosions from the Source Physics Experiment: Theory

Author(s): Carmichael, Joshua Daniel
Snelson-Gerlicher, Catherine Mary

Intended for: Report

Issued: 2015-07-29

Azimuthal Sampling of Tectonic Release from Rayleigh Waves, Triggered by Shallow Explosions from the Source Physics Experiment: Theory

Joshua D Carmichael [1], Cathy Snelson [2]

July 28, 2015

[1]EES-17, Geophysics. Los Alamos National Laboratory, Los Alamos NM, USA
[2]EES-17, Geophysics. Los Alamos National Laboratory, Los Alamos NM, USA; Formerly at National Security Technologies, LLC. (NSTec), Las Vegas, NV 89193-8521

Contents

List of Figures

0.1 Abstract

Underground explosions often produce Rayleigh waves with non-circular radiation patterns. The presence of significant anisotropic radiation patterns from isotropic sources is often attributed to the coincident release of tectonic strain across faults that are spatially near the explosion working point. However, poor instrument deployment geometries can lead to misinterpretations of these fields as isotropic when the are non-circular. In this work, we construct a physical representation for the first two moments of the Rayleigh wave radiation pattern triggered by a shallow, underground explosion. We then construct a hypothesis test for discriminating between the isotropic and anisotropic portion of the radiated Rayleigh wavefield, using these moments. We find that the screening power is completely quantified by a single parameter λ that depends on azimuthal deployment geometry as well as wavefield sampling. To improve radiation pattern discrimination, we present an algorithm for iteratively including receivers to sample the radiation pattern that increases the performance (power) of the hypothesis test at each iteration. Last, we discuss future applications of our method to data recorded from the Source Physics Experiment taking place at the Nevada National Security Site (NNSS).

1.1 Introduction

Several decades of seismic observations recorded from shallow, underground explosions have revealed that so-called isotropic sources produce Love waves and Rayleigh waves with non-circular radiation patterns. These observations generally contrast with traditional physical models that predict an absence of Love waves, and azimuthally constant Rayleigh wave amplitudes. The non-circular component of Rayleigh wave radiation patterns, in particular, has been physically attributed to what is known as tectonic release [3], and more recently, damage production [14, 15, 18]. Tectonic release describes the coincident, or nearly coincident, release of tectonic strain triggered by the outgoing shock of an underground explosion [3]. The effective fault plane facilitating this release can then induce a non-circular radiation pattern component to the observed surface-wave field. Damage describes host medium changes induced by the outgoing, explosively driven shock and following wavefield interference. Initial damage produced by the incident shock creates a shatter zone in the host medium, and the later, free-surface stress wave rebound induces heaving and material bulking. These cumulative processes contribute a compensated, linear vector dipole (CLVD) and general double couple portion to the seismic moment tensor and Rayleigh wave radiation pattern.

One challenge associated with observing non-isotropic Rayleigh wave radiation patterns is determining when deviations from a circular pattern are significant. This level of significance is largely determined by the azimuthal sampling of the pattern. Ideally, any seismic observations will include a complete azimuthal sampling of the ground displacement. In reality, topography or other physical or logistical restrictions may impede sufficient sampling. This is important because uneven sampling can bias the estimated damage or tectonic components. For example, records collected near pattern nodes will negatively bias the estimated pattern anisotropy, while sampling only the maxima of an earthquake-like radiation pattern of "petals" positively biases the perceived isotropic component. Deploying additional, supplemental instruments at certain azimuthal gaps may then improve the non-optimal sampling of this pattern.

Answering these questions requires (1) constructing the right experiment, and (2) formulating an evaluable hypothesis test. This first point can be addressed by the Source Physics Experiment (SPE). These experiments comprise a campaign of underground explosive tests at the Nevada National Security Site (NNSS) designed to provide data necessary for developing more physics-based nuclear test monitoring tools [20] (Figure 1.1 shows a current instrument deployment map at five distinct azimuths). The second point can be addressed using binary hypothesis testing. Such testing describes the process of comparing two probability density functions of a test statistic for two competing models, often described as signal-absent versus signal present [8, 9]. Our present goal is develop a theory that will determine what azimuthal (instrument) sampling of an explosively-generated Rayleigh wave radiation pattern, in addition to one already present (e.g., Figure 1.1), will best determine if that explosion accompanies tectonic release. To achieve this goal, we use concepts from detection theory and experiment design to provide an algorithm that provides an optimal, supplemental deployment azimuth for additional instruments.

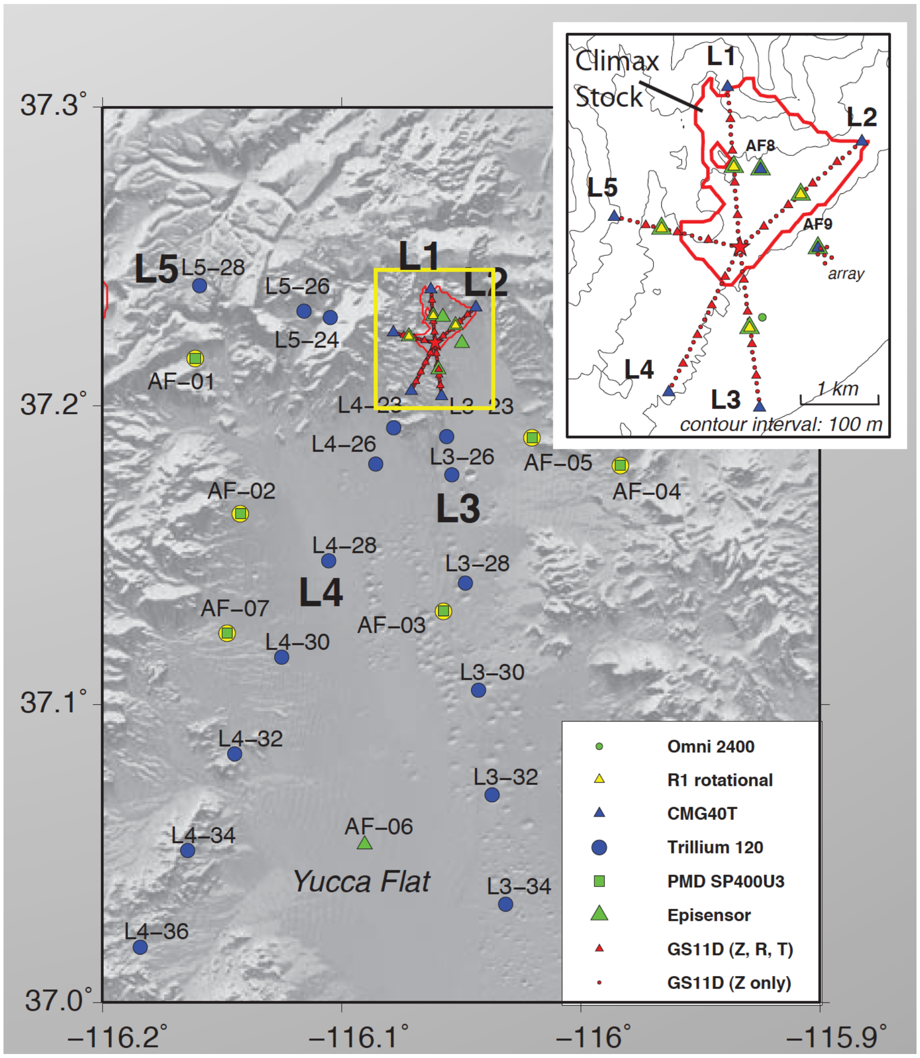

Figure 1.1: Deployment geometry of seismic instruments for the Source Physics Experiment at the Nevada National Security Site (NNSS) includes five primary lines of instruments, at five distinct azimuths, deployed at increasing distance from working point. Instruments considered here are three component seismometers (yellow triangles, inset; figure after William Walter, Lawrence Livermore National Laboratory).

1.2 Background

This section documents a physical theory that quantifies Rayleigh wave radiation patterns of shallow, buried explosions. Our initial presentation largely follows other's work [3], [15], [1] and exploits some material only referenced in exercises [1, 2002; pages 328-329], including equations which are not numbered. Unfortunately, some of this material includes typos. We therefore provide equivalent forms for the corrected equations here for reference. The expressions involving the moments of these radiation patterns, however, are original.

1.2.1 The Rayleigh Wave Radiation Pattern for a Near-Surface Explosion

The frequency-domain Rayleigh wave displacement field triggered by a shallow explosion with a symmetric moment tensor $\boldsymbol{M}$ is simplified from its general form (Aki and Richards, 2002, Eq. 7.151) when the source depth h is one-quarter or less of the dominant wavelength of the radiated field. In this case, the traction-free boundary conditions at the free surface for the displacement-traction vector $\boldsymbol{t} = (t_1,\ t_2,\ t_3,\ t_4)$ simplify the eigensolutions that compose the Rayleigh wave displacement field. This is because many of the eigensolution coefficients include tractions evaluated at the source working point, which is near the free surface. Speficially, these boundary conditions are (Aki and Richards, 2002, page 3.28):

$$
\begin{aligned}
t_3(h) &= \mu \left(\frac{dt_1}{dz} - kt_2 \right) \Bigg|_h = 0 \\
t_4\left(h\right) &= 0 \\
\mu \frac{dt_2}{dz}\bigg|_h &= \left(\frac{2\beta^2}{\alpha^2} - 1 \right) kt_1\left(h\right)
\end{aligned}
\tag{1.1}
$$

where α and β are the compressional and shear wave speed near the working point geology and k is the fundamental mode wavenumber. It follows from these boundary conditions that the Rayleigh wave displacement field $\boldsymbol{u}$ produced by a shallow source is expressible as:

$$
\boldsymbol{u} = \boldsymbol{G} \cdot \left[U_1 + U_2 \cos\left(2\phi\right) + U_3 \sin\left(2\phi\right)\right]. \tag{1.2}
$$

In Equation 1.2, $\boldsymbol{G}$ is the frequency-domain Rayleigh wave Green's function tensor, U_k ($k = 1, 2, 3$) are the radiation pattern coefficients that depend on the moment tensor components, and ϕ is the azimuthal angle (see Aki and Richards, 2002, Figure 4.20). The radiation pattern coefficients weighting the radiation functions in Equation 1.2 are given by:

$$
\begin{aligned}
U_1 &= \frac{1}{2}\left(M_{xx} + M_{yy}\right) - \left(\frac{2\beta^2}{\alpha^2} - 1 \right) M_{zz} \\
U_2 &= \frac{1}{2}\left(M_{xx} - M_{yy}\right) \\
U_3 &= M_{xy}
\end{aligned}
\tag{1.3}
$$

where M_{ij} is a moment tensor component for a force couple in direction i, separated by direction j. As a first example, we specifically consider the case that a shallow explosion with isotropic moment M_I accompanies a significant tectonic release with moment M_0 on a fault collocated or near the working point. We suppose this fault is parameterized by strike (ϕ_s), rake (λ) and dip (δ) angles. The radiation pattern coefficients are then expressible as (Aki and Richards, 2002, pg. 329):

$$\begin{aligned} U_1 &= \frac{2\beta^2}{\alpha^2} M_I - \frac{3\alpha^2 - 4\beta^2}{\alpha^2} DS \\ U_2 &= DS\cos(\phi_s) - SS\sin(\phi_s) \\ U_3 &= SS\cos(\phi_s) + DS\sin(\phi_s) \end{aligned} \tag{1.4}$$

In Equation 1.4, SS is a scalar that quantifies the strength of the strike-slip component of the tectonic release, and DS quantifies the corresponding strength of the dip slip component. The tectonic release terms are defined by [3, Equations 21, 22]:

$$\begin{aligned} DS &= \frac{1}{2} M_0 \sin(2\delta)\sin(\lambda) \\ SS &= M_0 \sin(\delta)\cos(\lambda) \end{aligned} \tag{1.5}$$

We note that the equivalent expression in Patton and Taylor [15, Equation 16] is missing a factor of two scaling the dip angle included in the DS term, but was likely a typo. Regardless, we express the full Rayleigh wave displacement by combining the fault-plane expressions for the radiation pattern in Equations 1.4 and 1.5 with Equation 1.2:

$$\boldsymbol{u} = \boldsymbol{G} \cdot [U_1 + DS\cos(2(\phi - \phi_s)) + SS\sin(2(\phi - \phi_s))] \tag{1.6}$$

Equations 1.4 and 1.5 illustrate that a purely volumetric (explosive) source produces no azimuthal variation in the radiation pattern (e.g., $DS = SS = 0$ when $M_0 = 0$). These expressions additionally demonstrate that not all tectonic release fault planes will generate Rayleigh waves. In particular, a zero-degree dip angle with a zero rake angle (a vertical dip slip) produces no surface waves, while other fault geometries generate identical radiation patterns [2]. These properties are captured by the total radiation patten, which is expressible in the same form as the scalar function from Equation 1.2:

$$\mathcal{R} = U_1 + DS\cos(2\varphi) + SS\sin(2\varphi) \tag{1.7}$$

where φ is the difference between the azimuthal and strike angles. We use Equation 1.7 as a starting point for estimating optimal receiver sampling of the Rayleigh wave radiation pattern of a shallow explosion. Figure (2) illustrates the resultant, predicted radiation pattern normalized by total riggered by a shallow explosion in four parametric cases, for a normal fault; each radiation pattern is normalized by the total moment. This particular fault geometry maximizes the non-isotropic component of the radiation pattern.

1.2.2 Radiation Pattern Moments

To estimate ideal locations from which to measure variability in the Rayleigh wave radiation pattern for a buried, shallow explosive source, we determine (1) the root-mean-square (RMS) value of this radiation pattern and (2) its expected deviation from this mean. Our objective is to determine, for N observing receivers, what azimuthal coverage of supplemental instruments (say, $N+1$) at local and regional distances will provide the highest probability of correctly distinguishing the anisotropic portion of the radiation pattern.

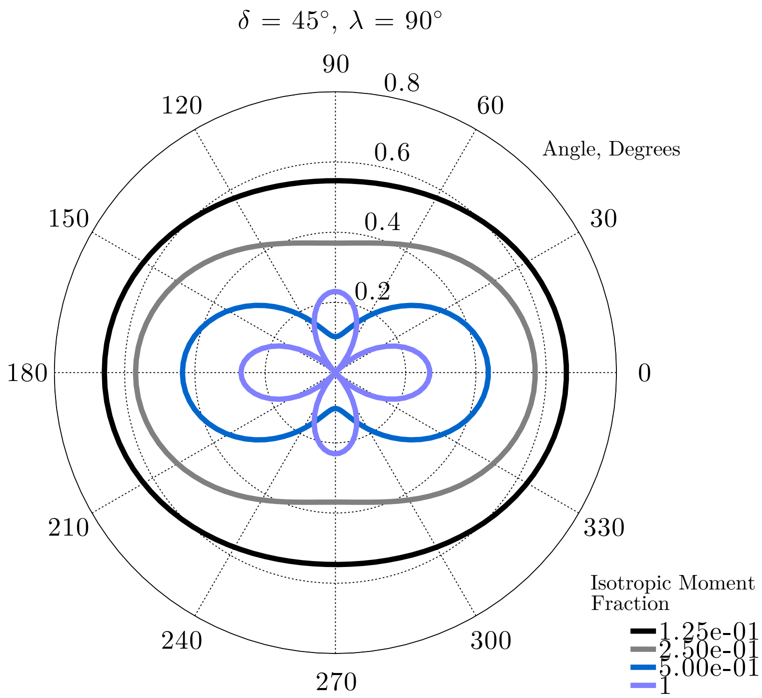

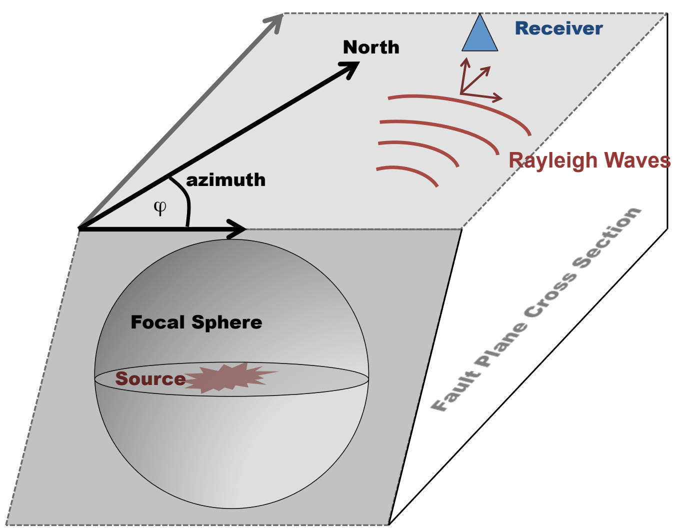

Figure 1.2: **Top**: Radiation patterns from a shallow explosion that is accompanied by normal faulting tectonic release, each normalized by the total seismic moment $M_I + M_0$. The labeled dip and rake angles correspond to Equation 1.5. We note that the four-lobe pattern dominates in cases where tectonic release is comparable to the explosion moment. **Bottom**: A notional description of an underground explosion, superimposed on a fault plane that releases tectonic strain upon detonation and radiates Rayleigh waves that are recorded in the far field by a three component receiver.

To compute the RMS radiation pattern $\bar{\mathcal{R}}$ for a near-surface source, we assume that the source (working point) is embedded in the surface of a layered half space, and surrounded by an imaginary, unit radii cylinder that extends into this space by the dominant wavelength L of the radiated elastic energy. We further assume that any tectonic release occurs over a fault with a strike angle of random orientation relative to North, e.g., the faults providing tectonic strain release are not preferentially oriented in a given direction. Under these two assumptions, we integrate the squared radiation pattern $\mathcal{R}$ over this cylinder, and normalize the integrand over the cylinder surface area; this process is exactly analogous to using Gaussian surfaces in electrostatics to compute properties of electric fields. In our case, this integrated radiation pattern is (Equation 1.7):

$$\bar{\mathcal{R}} = \frac{\sqrt{L \int_0^{2\pi} d\varphi \, [\, U_1 + DS\cos(2\varphi) + SS\sin(2\varphi)\,]^2}}{\sqrt{2\pi L}} \tag{1.8}$$

The radiation coefficient weights $[1, \cos(2\varphi), \sin(2\varphi)]$ in Equation 1.8 are mutually orthogonal (e.g., statistically independent) over the azimuthal interval $[0, 2\pi]$. This means that the integrands cross terms, such as $DS\cos(2\varphi) \cdot SS\sin(2\varphi)$, integrate to zero. Integrating the remaining terms and performing additional arithmetic simplification, we reduce Equation 1.8 to:

$$\bar{\mathcal{R}} = \sqrt{U_1^2 + \frac{1}{2}(DS^2 + SS^2)} \tag{1.9}$$

The expression in Equation 1.9 does not completely quantify the mean radiation pattern. In particular, explosions with sub-horiztonal tectonic release of moment $M_0^{(1)}$ will deviate from this RMS pattern more than a similar explosion with smaller tectonic release $M_0^{(2)}$, if $M_0^{(1)} > M_0^{(2)}$. To quantify this deviation, we compute the second moment of the radiation pattern, averaged over the same "Gaussian" cylinder:

$$\sigma_{\mathcal{R}} = \frac{\sqrt{L \int_0^{2\pi} d\varphi \left[U_1 + DS\cos(2\varphi) + SS\sin(2\varphi)\; - \bar{\mathcal{R}} \right]^2}}{\sqrt{2\pi L}} \tag{1.10}$$

This integral has the same basic form as the integral for $\bar{\mathcal{R}}$ (Equation 1.8). In this case, the azimuthally independent term is $U_1 - \bar{\mathcal{R}}$. We again utilize basis function orthogonality over azimuthal range and obtain:

$$\sigma_{\mathcal{R}} = \sqrt{\left(U_1 - \bar{\mathcal{R}}\right)^2 + \frac{1}{2}(DS^2 + SS^2)} \tag{1.11}$$

We now consider both the RMS and deviation terms in the specific case of a pure explosion, e.g., where tectonic release is absent ($M_0 = 0$). We first note that the radiation pattern completely isotropic and independent of azimuth:

$$\bar{\mathcal{R}}\big|_{M_0=0} = U_1\big|_{M_0=0} = \frac{2\beta^2}{\alpha^2} M_I \tag{1.12}$$

This expression applies to vertical dip slip faults as well, since they generate no surface waves [3]. Because the total radiation pattern for explosions and vertical dip slip faulting equates the RMS value in Equation 1.12, the associated second moments are both zero:

$$\sigma_{\mathcal{R}}\big|_{M_0=0} = 0 \tag{1.13}$$

These moments will be important for comparing different radiation pattern hypotheses in the following sections. In particular, we note that if Rayleigh waves are set up by an explosion that accompanies a non-vertical dip slip component of tectonic release, then both the first and second moments of $\mathcal{R}$ ($\bar{\mathcal{R}}$ and $\sigma_{\mathcal{R}}$) increase in ratio relative to their explosion-only zero value. In Section .1.1 (Appendix A), we demonstrate that the ratio of $\sigma_{\mathcal{R}}$ to $\bar{\mathcal{R}}$, for "almost" isotropic radiation patterns scales like $\dfrac{M_0}{M_I}$, and increases most rapidly for strike slip tectonic faulting. This suggests that $\bar{\mathcal{R}}$ alone is insufficient to screen isotropic from anisotropic explosion radiation patterns.

Figure 1.3 shows radiation patterns superimposed with their RMS and RMS-deviated values for several ratios of isotropic to tectonic release moment, $\frac{M_0}{M_I}$, computed for several different faults. A normal faulting case, where $\delta = 45°$ and $\lambda = 90°$, shows the greatest deviation from a circular pattern. Despite this variability, the illustrated Rayleigh wavefield is misinterpretable as isotropic with non-optimal instrument deployment, even with equal isotropic and tectonic moments. In particular, if such a radiation pattern were produced by an explosion, and instruments were deployed at four locations such that the strike-minus-azimuth angles were $\pm 153.5°$ and $\pm 23.6°$, they would coincidentally sample locations at which this pattern equated its RMS values. A more optimal deployment scheme would sample the lobe peaks and nodes.

1.3 Hypothesis Testing

To determine if the Rayleigh wave radiation pattern includes tectonic release, we evaluate a hypothesis test that compares two distinct models for $\mathcal{R}$. This test requires forming a test statistic using N observations of $\mathcal{R}$ at different azimuthal locations, in a maximum likelihood sense. Our "null" hypothesis is that an azimuthally distributed set of sensors samples an isotropic, or circularly symmetric radiation pattern. Our alternative hypothesis

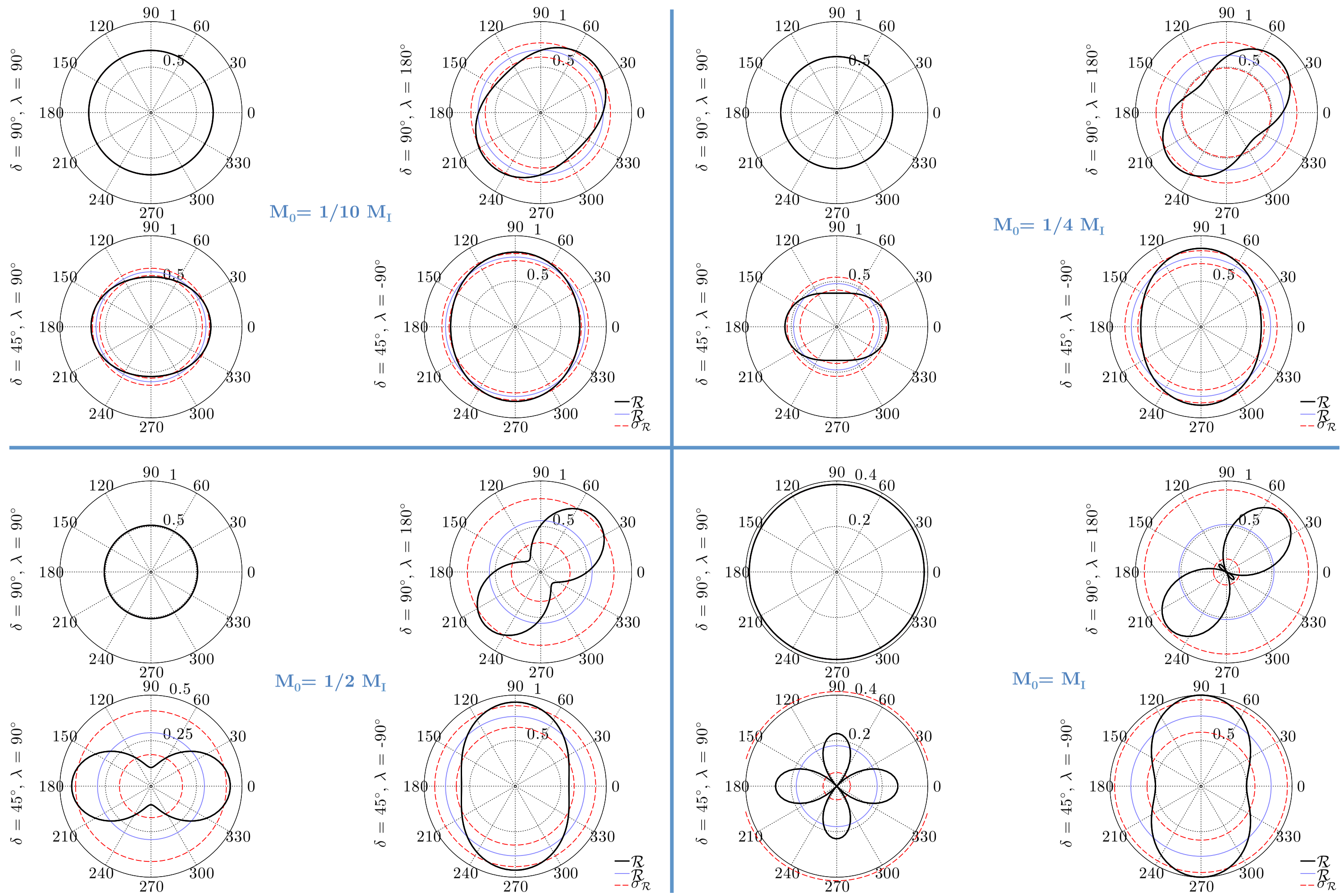

Figure 1.3: Radiation patterns and first two pattern moments for four different faulting geometries of tectonic release and four distinct ratios of isotropic to tectonic release moments (M_I/M_0). Moment ratio panels are separated by thick, blue lines. Each panel (e.g., top left, $M_0 = \frac{1}{10}M_I$) shows Rayleigh wave radiation patterns (black curves) with their RMS values $\bar{\mathcal{R}}$ (purple curves), superimposed with $\bar{\mathcal{R}} \pm \sigma_{\mathcal{R}}$ (red, dashed lines). All patterns are scaled by the total moment ($M_0 + M_I$).

is that these same sensors sample a non-circular radiation pattern. We state these two hypothesis as:

$$\begin{aligned} \mathcal{H}_0 : &\quad \mathcal{R} = \bar{\mathcal{R}}\big|_{M_0=0} \\ \mathcal{H}_1 : &\quad \mathcal{R} = U_1 + DS\cos(2\varphi) + SS\sin(2\varphi) \quad (\delta,\ \lambda,\ M_0 \text{ unknown}) \end{aligned} \tag{1.14}$$

We assume that M_I has been estimated from data using body wave data and therefore includes negligible model error, e.g., M_0 contributes little to the total solution for M_I. We may include model errors in future work. At present, we continue with this assumption, and introduce a probability model for the estimate of M_I. This model is necessary, since observations of moments are not deterministic, but measured from imperfect and/or noisy data. Following several others [13, 16, 17, 11, 12], we assume that magnitudes are normally distributed so that the isotropic moment M_I is also log-normally distributed. This assumption is further substantiated by both modeling and empirical observations [5, 7, 6], *if moment is estimated from station magnitudes.* If isotropic moment is instead estimated from the trace of a moment tensor inversion, ($M_I = \frac{1}{3}\mathrm{tr}\,(\boldsymbol{M})$) then the non-deterministic uncertainty in that estimate appears Gaussian under rather general conditions [10]. Further, normally distributed errors often dominate seismic waveform records that are compared against synthetic seismograms to estimate isotropic scalar moments [19, 4, 21]. Such waveform noise does not necessarily dominate the uncertainty in moment tensor calculations. This is because many source parameters are often unknown, including source hypocenters and focal mechanisms. In addition, the velocity structure needed to construct the Rayleigh wave Green's eigenfunctions is often imperfectly known. In the SPE experiments we consider here, both source location and source type (minus any tectonic release) are known. In addition, the geology of the Nevada National Security Site is (relatively) well characterized. Therefore, two components of deterministic error, normally dominant in uncontrolled experiments, are greatly reduced for the SPE shots. Therefore, we consider waveform noise to be a dominant source of random error in the moment estimates and model the scalar moment as a normally distributed random variable. Notationally, we denote an observed value of $\frac{2\beta^2}{\alpha^2}M_I$ with mean μ_M and variance σ_M^2 as $\frac{2\beta^2}{\alpha^2}M_I \sim \mathcal{N}\left(\mu_M, \sigma_M^2\right)$. While the true variance σ_M^2 is unknown, it is constrained much better than the focal planes characterized by DS and SS that provide tectonic release. In Appendix .1, we demonstrate that for small values of $\mathcal{R}$, the second moment of $\mathcal{R}$ changes slowly relative to changes in its RMS values so that $\frac{\sigma_{\mathcal{R}}}{\bar{\mathcal{R}}} \propto \frac{M_0}{M_I}$. We therefore suggest that sources of bias in estimates of σ_M are small relative bias from other source, and take σ_M to be independent of the fault plane model. This means that the statistical behavior in radiation pattern is approximately linear in it's parameters. To then exploit this model, we more explicitly express the hypotheses in Equation 1.14 in terms of moment, using Equations 1.7 and 1.12:

$$
\begin{aligned}
&\mathcal{H}_0: \ \mathcal{R} = \frac{2\beta^2}{\alpha^2}M_I \\
&\mathcal{H}_1: \ \mathcal{R} = \frac{2\beta^2}{\alpha^2}M_I - \frac{3\alpha^2 - 4\beta^2}{\alpha^2}DS + DS\cos(2\varphi) + SS\sin(2\varphi) \quad (M_I,\, DS,\, SS \text{ unknown})
\end{aligned}
\tag{1.15}
$$

where we have noted that the unknown parameters δ, λ, M_0 are absorbed into coefficients DS, SS and cannot generally be separated without additional information [3]. Equation 1.15 is then equivalent to testing between two different probability distributions for $\mathcal{R}$:

$$
\begin{aligned}
\mathcal{H}_0 &: \ \mathcal{R} \sim \mathcal{N}\left(\mathbb{E}\left\{\frac{2\beta^2}{\alpha^2}M_I\right\}, \sigma_M^2\right) \\
\mathcal{H}_1 &: \ \mathcal{R} \sim \mathcal{N}\left(\mathbb{E}\left\{\frac{2\beta^2}{\alpha^2}M_I - \frac{3\alpha^2 - 4\beta^2}{\alpha^2}DS + DS\cos(2\varphi) + SS\sin(2\varphi)\right\}, \ \sigma_M^2\right)
\end{aligned}
\tag{1.16}
$$

where $\mathbb{E}\left\{\bullet\right\}$ is the expected value operator. Equation 1.16 is applicable to a single observation, or single azimuthal sample (say, φ_k). For a set of many observations, our hypothesis test instead includes a vectorized set of radiation pattern samples $\boldsymbol{\mathcal{R}}$ where the k^{th} sample is $\mathcal{R}_k$:

$$
\boldsymbol{\mathcal{R}} \triangleq \left[\mathcal{R}_1, \, \mathcal{R}_2, \, \cdots, \mathcal{R}_k, \, \cdots, \mathcal{R}_N\right]^{\mathrm{T}}. \tag{1.17}
$$

We additionally concatenate the unknown parameters M_I, SS, DS and σ_M into a single parameter vector:

$$
\boldsymbol{\theta} = \left[M_I, DS, SS, \sigma_M\right]^{\mathrm{T}}. \tag{1.18}
$$

The multivariate density function for the radiation pattern vector $\boldsymbol{\mathcal{R}}$ with mean vector $\boldsymbol{\mu}$ and covariance $\boldsymbol{C}$ is given by:

$$
f_{\boldsymbol{\mathcal{R}}}\left(\boldsymbol{\mathcal{R}}; \mathcal{H}_n\right) = (2\pi)^{-\frac{N}{2}} \left(\prod_{k=1}^{N} \mathcal{R}_k^{-1}\right) |\boldsymbol{C}|^{-\frac{1}{2}} \exp\left(-\frac{1}{2}(\boldsymbol{\mathcal{R}} - \boldsymbol{\mu})^{\mathrm{T}} \boldsymbol{C}^{-1} (\boldsymbol{\mathcal{R}} - \boldsymbol{\mu})\right). \tag{1.19}
$$

where $\mathcal{H}_n$ denotes the assumed hypothesis ($n = 0, 1$), component k of $\boldsymbol{\mu}$ is the vectorized true value of $\mathcal{R}$ (Equation 1.7) and $\boldsymbol{C}$ is an identify matrix weighted by σ_M^2. Under $\mathcal{H}_0$, DS and SS are each zero and $\mu_k = \mu_M \ \forall \ k$. To determine which hypothesis our data are most consistent with, we use a generalized log-likelihood ratio test. In simplest terms, this test compares the logarithmic ratio of the alternative hypothesis density function to the null hypothesis density function, where each function is respectively evaluated the maximum likelihood estimate (MLE) for it's unknown parameters. In our case, we posit that μ_M and variance σ_M^2 are substantially more constrained than SS and DS, and that the uncertainties in tectonic release parameters thereby dominant the shaping parameters for the distributions. The generalized log-likelihood ratio test is then:

$$L_{\boldsymbol{\theta}}(\boldsymbol{\mathcal{R}}) \underset{\mathcal{H}_0}{\overset{\mathcal{H}_1}{\gtrless}} \eta \quad \text{where:}$$
$$L_{\boldsymbol{\theta}}(\boldsymbol{\mathcal{R}}) = \ln\left[\frac{\max\limits_{\boldsymbol{\theta}|\mathcal{H}_1}\{\, f_{\boldsymbol{\mathcal{R}}}(\boldsymbol{\mathcal{R}};\mathcal{H}_1)\,\}}{\max\limits_{\boldsymbol{\theta}|\mathcal{H}_0}\{f_{\boldsymbol{\mathcal{R}}}(\boldsymbol{\mathcal{R}};\mathcal{H}_0)\,\}}\right] \tag{1.20}$$

where η is a to-be-determined threshold that quantifies a statistically significant departure from isotropic radiation (see Figure 1.4). The hypothesis $\mathcal{H}_0$ below the conditional inequality in Equation 1.20 signifies that $\boldsymbol{M}$ consists of log normal noise when $L_{\boldsymbol{\theta}}(\boldsymbol{\mathcal{R}}) < \eta$ and that the radiation pattern is isotropic; the hypothesis $\mathcal{H}_1$ signifies that $\boldsymbol{\mathcal{R}}$ includes a contribution from tectonic release if $L_{\boldsymbol{\theta}}(\boldsymbol{\mathcal{R}}) > \eta$. To apply the hypothesis test in Equation 1.20, we combine it with Equations 1.17, and 1.19. It follows that several terms in the ratio defining $L_{\boldsymbol{\theta}}(\boldsymbol{\mathcal{R}})$ arithmetically cancel, since:

$$\frac{\max\limits_{\boldsymbol{\theta}|\mathcal{H}_1}\{\, f_{\boldsymbol{\mathcal{R}}}(\boldsymbol{\mathcal{R}};\mathcal{H}_1)\,\}}{\max\limits_{\boldsymbol{\theta}|\mathcal{H}_0}\{f_{\boldsymbol{\mathcal{R}}}(\boldsymbol{\mathcal{R}};\mathcal{H}_0)\,\}} = \frac{\max\limits_{\boldsymbol{\theta}|\mathcal{H}_1}\left\{\exp\left(-\frac{1}{2\sigma_M^2}\left|\left|\boldsymbol{\mathcal{R}} - \boldsymbol{\mu}_1\right|\right|^2\right)\right\}}{\max\limits_{\boldsymbol{\theta}|\mathcal{H}_0}\left\{\exp\left(-\frac{1}{2\sigma_M^2}\left|\left|\boldsymbol{\mathcal{R}} - \boldsymbol{\mu}_0\right|\right|^2\right)\right\}} \tag{1.21}$$

where $\boldsymbol{\mu}_n$ is the mean vector for hypothesis $\mathcal{H}_n$, e.g., the expected value terms in Equation 1.16. The likelihood ratio is then maximized if the norm in the argument term of the

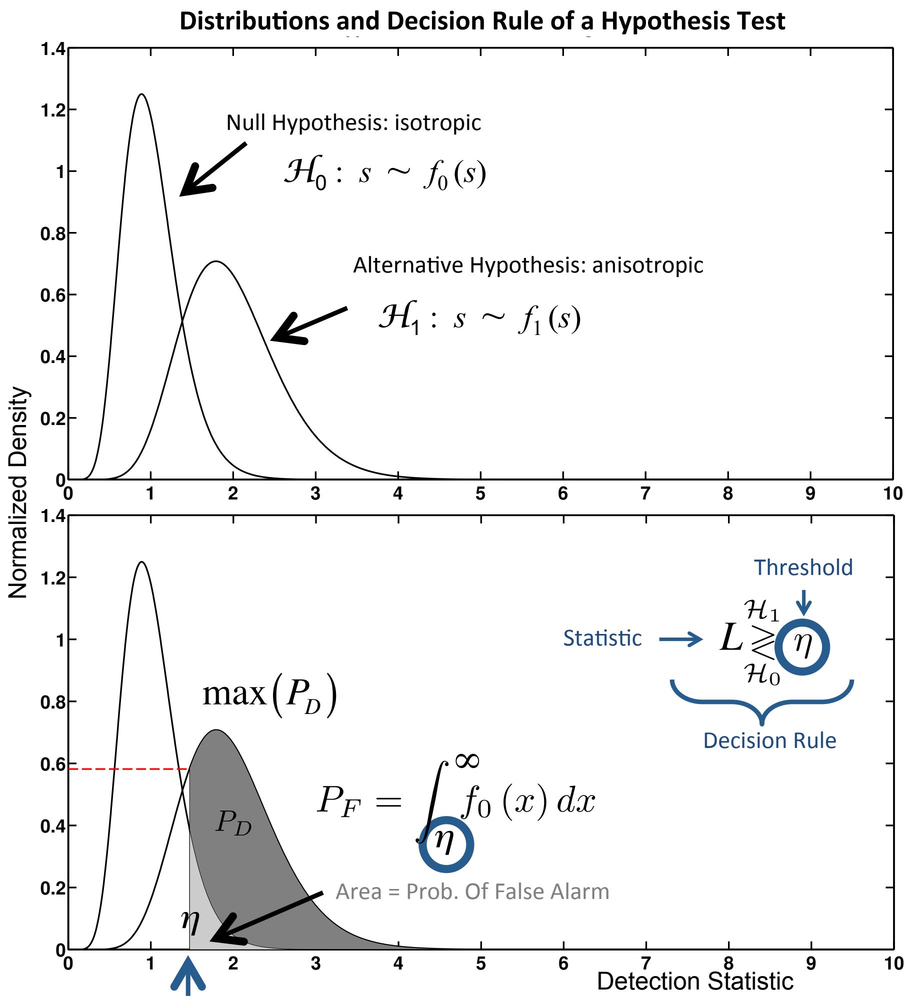

Figure 1.4: An illustration of the probability distribution distribution functions (PDFs) for a general (F-distributed) radiation screening statistic under two competing hypotheses. **Top**: Two competing hypothesis formed from an arbitrary scalar discrimination statistic. The left null distribution corresponds to a isotropic radiation pattern ($\lambda = 0$), whereas the right alternative distribution corresponds to anisotropic radiation ($\lambda > 0$). Overlap between the distributions implies that a high threshold is needed to avoid false source attribution, at the expense of mis-labeling an anisotropic explosion as isotropic. **Bottom**: Decision regions for the Neyman Pearson decision rule and partitioning by η. The shaded regions indicate the false attribution probability P_{FA} and the correct radiation discrimination probability P_D for this threshold choice. In both cases, the only difference between the null and alternative hypothesis density functions is the presence of a non-zero noncentrality parameter λ under $\mathcal{H}_1$

numerator is minimized:

$$\underset{\boldsymbol{\theta}}{\operatorname{argmax}}\left\{\exp\left(-\frac{1}{2\sigma_M^2}\left|\left|\boldsymbol{\mathcal{R}}-\boldsymbol{\mu}_1\right|\right|^2\right)\right\}=\underset{\boldsymbol{\theta}}{\operatorname{argmin}}\left\{\left|\left|\boldsymbol{\mathcal{R}}-\boldsymbol{\mu}_1\right|\right|^2\right\} \tag{1.22}$$

Thus, the maximum likelihood estimate for the unknown focal plane parameters minimizes the distance between the radiation pattern model $\boldsymbol{\mu}_1$ and the data $\boldsymbol{\mathcal{R}}$. The radiation pattern parameter solution is then a least-squares problem of the form $\underset{\boldsymbol{\theta}}{\min}\left|\left|\boldsymbol{\mathcal{R}}-\boldsymbol{H\theta}\right|\right|^2$. Under the alternative hypothesis ($\mathcal{H}_1$), this model is:

$$\boldsymbol{\mu}_1=\underbrace{\begin{bmatrix}1 & \cos(2\varphi_1) & \sin(2\varphi_1)\\ 1 & \cos(2\varphi_2) & \sin(2\varphi_2)\\ \vdots & \vdots & \vdots\\ 1 & \cos(2\varphi_k) & \sin(2\varphi_k)\\ \vdots & \vdots & \vdots\\ 1 & \cos(2\varphi_N) & \sin(2\varphi_N)\end{bmatrix}}_{\boldsymbol{H}}\cdot\underbrace{\begin{bmatrix}\frac{2\beta^2}{\alpha^2}M_I-\frac{3\alpha^2-4\beta^2}{\alpha^2}DS\\ DS\\ SS\end{bmatrix}}_{\boldsymbol{\theta}} \tag{1.23}$$

Using the notation in Equation 1.4, the parameter vector estimate is then the least squares solution:

$$\hat{\boldsymbol{\theta}}=[\boldsymbol{H}^{\mathrm{T}}\boldsymbol{H}]^{-1}\boldsymbol{H}^{\mathrm{T}}\boldsymbol{\mathcal{R}} \tag{1.24}$$

This solution requires that each trigonometric function includes a known azimuthal angle. In our example, $N=5$, corresponding to the equidistant receivers along the distinct azimuthal lines in Figure .1.1. Using the solution in Equation 1.24 for $\boldsymbol{\theta}$, we compute the maximum likelihood statistics for the variances under each hypothesis and use properties of projector matrices to reduce the resultant discrimination statistic to (algebra omitted):

$$L_{\boldsymbol{\theta}}\left(\boldsymbol{\mathcal{R}}\right) = \left(\frac{N-3}{3}\right) \cdot \frac{\left\|\boldsymbol{P_H}\boldsymbol{\mathcal{R}}\right\|^2}{\left\|\boldsymbol{P}_{\boldsymbol{H}}^{\perp}\boldsymbol{\mathcal{R}}\right\|^2} \tag{1.25}$$

In Equation 1.25, $\boldsymbol{P_H}$ is the orthogonal projector matrix that projects vectors onto the subspace spanned by the columns of $\boldsymbol{H}$ and $\boldsymbol{P}_{\boldsymbol{H}}^{\perp}$ is it's orthogonal complement, that projectors vectors onto the space orthogonal to that spanned by $\boldsymbol{H}$. The random variable $L_{\boldsymbol{\theta}}\left(\boldsymbol{\mathcal{R}}\right)$ has a central F distribution with 3 and $N-3$ degrees of freedom under the null (isotropic) case. Under the anisotropic case, it has a noncentral F distribution with the same pair of degrees of freedom, but with a noncentrality parameter given by :

$$\lambda = \frac{\left\|\boldsymbol{P_H}\boldsymbol{\mu}_1\right\|^2}{\sigma_M^2} \tag{1.26}$$

This scalar quantifies the discrimination power between the two competing hypotheses. A large value of λ, relative to smaller values, increases the screening power of the statistical test described by Equation 1.20 (Figure 1.4). This value obviously depends on the specific construction of $\boldsymbol{H}$. Adding receivers at certain azimuthal angles in the field is equivalent to including additional rows of the form $[1, \cos(2\varphi_k), \sin(2\varphi_k)]$ to the columns of $\boldsymbol{H}$ (for some k). Therefore, to optimally decide if a Rayleigh wave radiation pattern is anisotropic, instruments should be deployed in such a way that λ is maximized over all possible values of φ. Because μ_1 is unknown, this problem cannot be directly solved. Rather, it is approximately solvable using the maximum likelihood estimate for $\boldsymbol{\mu}_1$, given by $\hat{\boldsymbol{\mu}}_1 = \boldsymbol{H}\hat{\boldsymbol{\theta}}$, which includes components of $\boldsymbol{\mathcal{R}}$. We then select a desired value of $\mathcal{R}$ to sample. Since we have established that an explosively-triggered Rayleigh wave radiation pattern is expected to vary from it's RMS value only for non-isotropic moment tensors, we choose to sample $\bar{\mathcal{R}} + \sigma_{\mathcal{R}}$. Since the true value of $\bar{\mathcal{R}}$ is also unknown, it must be estimated using Equations 1.4

and 1.9 and the parameter estimate $\hat{\boldsymbol{\theta}}$. With these estimates, the problem required to find an approximately optimal value of φ for the $(N+1)^{\text{th}}$ receiver to supplement an existing array of N receivers, is:

$$\varphi_{N+1} = \underset{\varphi|\mathcal{H}_1}{\operatorname{argmax}} \left\{ \frac{\left\| \boldsymbol{H}_1 \cdot ([\boldsymbol{H}_1^{\mathrm{T}} \boldsymbol{H}_1]^{-1} \boldsymbol{H}_1^{\mathrm{T}})^2 \cdot \boldsymbol{\mathcal{R}}_1 \right\|^2}{\hat{\sigma}_M^2} \right\} \tag{1.27}$$

where $\hat{\sigma}_M^2$ is a variance estimate for $\dfrac{2\beta^2}{\alpha^2} M_I$ and $\boldsymbol{H}_1$ and $\boldsymbol{\mathcal{R}}_1$ are defined by:

$$\underbrace{\begin{bmatrix} \boldsymbol{\mathcal{R}} \\ \bar{\mathcal{R}} + \sigma_{\mathcal{R}} \\ \vdots \\ \bar{\mathcal{R}} + \text{value} \end{bmatrix}}_{\boldsymbol{\mathcal{R}}_j} = \underbrace{\begin{bmatrix} & \boldsymbol{H} & \\ 1 & \cos(2\varphi_{N+1}) & \sin(2\varphi_{N+1} \\ \vdots & \vdots & \vdots \\ 1 & \cos(2\varphi_{N+j}) & \sin(2\varphi_{N+j}) \end{bmatrix}}_{\boldsymbol{H}_j} \cdot \underbrace{\begin{bmatrix} \hat{\theta}_1 \\ \hat{\theta}_2 \\ \hat{\theta}_3 \end{bmatrix}}_{\boldsymbol{\theta}} \tag{1.28}$$

In this case, $j = 1$. Additional rows are iteratively computed, as described below. The term "value" in the last row indicates a constraint imposed by the user that must be within the range of deviation from possible RMS values.

In practice, we recommend the application of computational tools to implement Equation 1.27 (like Matlab's `fminsearch.m`) and thereby estimate optimal values for φ_{N+1}. For additional receiver deployments, say φ_{N+2}, Equation 1.27 must be applied iteratively. Starting with Equation 1.4, the psuedo code for estimating the quasi-optimal distribution of receivers for discriminating between isotropic and anisotropic Rayleigh wave radiation is:

for $k = 1{:}N$,

1. Estimate $\hat{\boldsymbol{\theta}}$ from Equations 1.4 and 1.24;
2. Recompute $\bar{\mathcal{R}}$ and $\sigma_{\mathcal{R}}$ from Equations 1.9 and 1.11 using equivalent sample averages (in place of integrals).
3. Reform matrices $\boldsymbol{\mathcal{R}}_{k-1}$ and $\boldsymbol{H}_{k-1}$ using Equation 1.28
4. Solve for an the optimal azimuthal angle for receiver $N+\ k$ using Equation 1.27

end;

1.4 Discussion and Future Application

We summarize the three most important aspects of the current work below:

- Section 1.2.2, documents approximate physical moments for the Rayleigh wave radiation pattern produced by a shallow, buried explosion accompanied with some form of tectonic release. These moments give the RMS radiation pattern and the expected deviation from the RMS value. We find that for slightly non-isotropic explosions, dip, rake angle pairs of ($\delta = 45°$, $\lambda = 90°$) (normal faulting) differ most from purely isotropic explosions. However, even these cases can lead to misidentification. In cases where fault strike angle is know *apriori*, instruments should be deployed along radiation pattern lobes least likely to sample radiation patterns that equate to the RMS values. In the normal faulting case above, the least optimal deployment angles include where the strike and instrument azimuth differences are $\pm 153.5°$ and $\pm 23.6°$, where $\bar{\mathcal{R}} = \mathcal{R}$.
- Section 1.3 documents the hypothesis test used to quantify an optimality criteria

for testing between isotropic radiation present versus anisotropic radiation absent. We find that the discrimination performance is entirely quantified by a so called noncentrality parameter that shapes the anisotropic radiation present distribution, under $\mathcal{H}_1$, given by 1.26. This scalar parameter depends on azimuthal sampling of seismic receivers that measure the Rayleigh wave radiation field, and the field itself.

- Section 1.3 also documents the iterative algorithm (in pseudo-code) that we recommend and will use to estimate the optimal receiver deployment geometry in additional phases of SPE deployments.

The data required to implement Equation , such as scalar moment estimates and moment tensor inversion components, is currently being processed by David Yang at Los Alamos National Laboratory. Our anticipated results will be provided by September 15, 2015.

Bibliography

[1] Keiti Aki and Paul G. Richards. *Quantitative Seismology.* University Science Books, Sausalito, CA, USA, 2nd edition, 2002.

[2] BG Bukchin. Specific features of surface wave radiation by a shallow source. *Izvestiya, Physics of the Solid Earth*, 42(8):712–717, 2006.

[3] Gran Ekström and Paul G. Richards. Empirical measurements of tectonic moment release in nuclear explosions from teleseismic surface waves and body waves. *Geophysical Journal International*, 117(1):120–140, 1994.

[4] Sean R Ford, Douglas S Dreger, and William R Walter. Identifying isotropic events using a regional moment tensor inversion. *Journal of Geophysical Research: Solid Earth (1978–2012)*, 114(B1), 2009.

[5] C Godano and F Pingue. Is the seismic moment–frequency relation universal? *Geophysical Journal International*, 142(1):193–198, 2000.

[6] Yan Y Kagan. Seismic moment distribution revisited: I. statistical results. *Geophysical Journal International*, 148(3):520–541, 2002.

[7] YY Kagan. Seismic moment distribution. *Geophysical Journal International*, 106(1):123–134, 1991.

[8] Steven M. Kay. *Fundamentals of Statistical Signal Processing: Estimation Theory.* Prentice-Hall Inc., Upper Saddle River, New Jersey, USA, 1st edition, 1993.

[9] Steven M. Kay. *Fundamentals of Statistical Signal Processing: Detection Theory.* Prentice-Hall Inc., Upper Saddle River, New Jersey, USA, 1st edition, 1998.

[10] Dana Křížová, Jiří Zahradník, and Anastasia Kiratzi. Resolvability of isotropic component in regional seismic moment tensor inversion. *Bulletin of the Seismological Society of America*, 103(4):2460–2473, 2013.

[11] Tormod Kværna and Frode Ringdal. Seismic threshold monitoring for continuous assessment of global detection capability. *Bulletin of the Seismological Society of America*, 89(4):946–959, 1999.

[12] Tormod Kværna and Frode Ringdal. Detection capability of the seismic network of the international monitoring system for the comprehensive nuclear-test-ban treaty. *Bulletin of the Seismological Society of America*, 103(2A):759–772, 2013.

[13] Jonathan K MacCarthy, Dale N Anderson, and Jessie L Bonner. Combined rayleigh- and love-wave magnitudes for seismic event discrimination and screening analysis. *Bulletin of the Seismological Society of America*, 103(6):3334–3340, 2013.

[14] Howard J Patton and Steven R Taylor. Effects of shock-induced tensile failure on mb-ms discrimination: Contrasts between historic nuclear explosions and the north korean test of 9 october 2006. *Geophysical Research Letters*, 35(14), 2008.

[15] Howard J. Patton and Steven R. Taylor. The apparent explosion moment: Inferences of volumetric moment due to source medium damage by underground nuclear explosions. *Journal of Geophysical Research: Solid Earth*, 116(B3):n/a–n/a, 2011. B03310.

[16] Frode Ringdal. Estimation of seismic detection thresholds. *Bulletin of the Seismological Society of America*, 65(6):1631–1642, 1975. PT: J; NR: 15; TC: 28; J9: B SEISMOL SOC AM; PG: 12; GA: BE659; UT: WOS:A1975BE65900007.

[17] Frode Ringdal and Tormod Kværna. Continuous seismic threshold monitoring. *Geophysical Journal International*, 111(3):505–514, 1992.

[18] Esteban Rougier and Howard J Patton. Seismic source functions from free-field ground motions recorded on spe: implications for source models of small, shallow explosions. *Journal of Geophysical Research: Solid Earth*, 2015.

[19] J Šílenỳ, P Campus, and GF Panza. Seismic moment tensor resolution by waveform inversion of a few local noisy recordsi. synthetic tests. *Geophysical Journal International*, 126(3):605–619, 1996.

[20] Catherine M Snelson, Robert E Abbott, Scott T Broome, Robert J Mellors, Howard J Patton, Aviva J Sussman, Margaret J Townsend, and William R Walter. Chemical explosion experiments to improve nuclear test monitoring. *Eos, Transactions American Geophysical Union*, 94(27):237–239, 2013.

[21] Fabian Walter, John F. Clinton, Nicholas Deichmann, Douglas S. Dreger, Sarah E. Minson, and Martin Funk. Moment Tensor Inversions of Icequakes on Gornergletscher, Switzerland. *Bulletin of the Seismological Society of America*, 99(2):852–870, 2009.

.1 Approximations

Our primary focus is testing difficult-to-discriminate radiation patterns against the isotropic radiation hypothesis. We therefore do not treat radiation patterns that are well sampled and obviously contain some form of tectonic release or damage-production that induces lobes to the Rayleigh wave field. Instead, we focus on cases where noise present in the data may be misinterpreted as tectonic release, or, where true tectonic release is incorrectly interpreted as noise.

We therefore assume, hereon, that $M_0 \ll M_I$.

.1.1 The Radiation Pattern Coefficient of Variation

For values of tectonic release moment (M_0) that are small relative to isotropic moment (M_I), the RMS Rayleigh radiation pattern is well approximated by a linearization about $M_0 = 0$:

$$\begin{aligned}
\bar{\mathcal{R}} &= \sqrt{U_1^2 + \frac{1}{2}(DS^2 + SS^2)} \\
&\approx \bar{\mathcal{R}}\big|_{M_0=0} + \frac{\partial \bar{\mathcal{R}}}{\partial M_0}\big|_{M_0=0}(M_0 - 0) \quad \text{(if: } M_0 \ll M_I) \\
&= \bar{\mathcal{R}}\big|_{M_0=0} + \frac{1}{4U_1}\Big|_{M_0=0}\left(DS^2 + SS^2\right) \\
&= \frac{2\beta^2}{\alpha^2}M_I + \frac{\alpha^2}{8M_I\beta^2}\left(DS^2 + SS^2\right) \\
&= \frac{2\beta^2}{\alpha^2}M_I + \frac{\alpha^2}{8\beta^2}\cdot\frac{M_0^2}{M_I}\left(\sin^2(\delta)\cos^2(\lambda) + \frac{1}{4}\sin^2(2\delta)\sin^2(\lambda)\right),
\end{aligned} \tag{.1.1}$$

where we have used Equation 1.12 and expanded the $\frac{1}{2}\left(DS^2 + SS^2\right)$ term. We note that the leading term in this approximation is of order M_I while the following terms is of order M_0^2/M_I. Thus, we neglect this term and posit that:

$$\bar{\mathcal{R}} \approx \frac{2\beta^2}{\alpha^2} M_I \tag{.1.2}$$

to first order. This is consistent with our modeling results in Figure 1.3 for $M_0 \leq \frac{1}{10} M_I$. We cannot similarly approximate the $\sigma_{\mathcal{R}}$ term using a Taylor series since both the first coefficient is zero and the gradient term is undefined at $M_I = 0$. We therefore approximate the term $\left(U_1 - \bar{\mathcal{R}}\right)/M_I$ by noting that it includes terms of order M_0/M_I and M_0^2/M_I^2, and neglect the second order terms:

$$\begin{aligned} M_I \cdot \sigma_{\mathcal{R}} &= \sqrt{\left(\frac{U_1 - \bar{\mathcal{R}}}{M_I}\right)^2 + \frac{1}{2}\left(\frac{DS^2 + SS^2}{M_I^2}\right)} \\ &\approx \sqrt{\frac{7\alpha^2 - 8\beta^2}{2\alpha^2}\left(\frac{DS}{M_I}\right)^2 + \frac{1}{2}\left(\frac{DS^2 + SS^2}{M_I^2}\right)} \end{aligned} \tag{.1.3}$$

This gives:

$$\begin{aligned} \sigma_{\mathcal{R}} &\approx \frac{1}{\sqrt{2}}\sqrt{SS^2 + \gamma \cdot DS^2} \\ &= \frac{1}{\sqrt{2}} M_0 \sqrt{\sin^2(\delta)\cos^2(\lambda) + \frac{\gamma}{4}\sin^2(2\delta)\sin^2(\lambda)} \end{aligned} \tag{.1.4}$$

where:

$$\gamma = \left(\frac{7\alpha^2 - 8\beta^2}{\alpha^2}\right). \tag{.1.5}$$

The ratio of the second to first moment (coefficient of variation) is then directly proportional to the ratio of the tectonic moment to isotropic moment:

$$\frac{\sigma_{\mathcal{R}}}{\bar{\mathcal{R}}} \approx \frac{\alpha^2}{\sqrt{8}\beta^2}\frac{M_0}{M_I}\sqrt{\sin^2(\delta)\cos^2(\lambda) + \frac{\gamma}{4}\sin^2(2\delta)\sin^2(\lambda)} \tag{.1.6}$$

The angular function weighting this coefficient of variation, or CV, is maximized for strike slip faults, in addition to other non-unique combinations of fault angles (Figure .1.1).

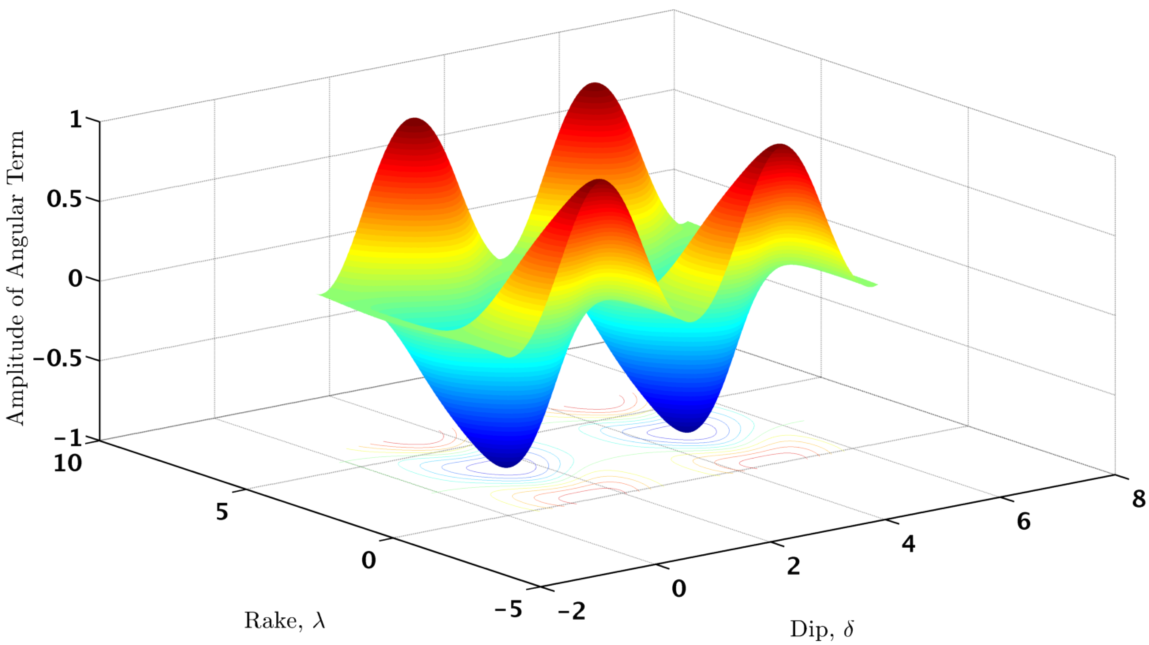

Figure .1.1: The angular function weight for the term $\frac{\sigma_{\mathcal{R}}}{\bar{\mathcal{R}}}$ in Equation .1.6, which holds for small amounts of tectonic release.